

Porous nanostructured metal oxides synthesized through atomic layer deposition on a carbonaceous template followed by calcination

Shaoren Deng,^{‡, a} Mert Kurttepli,^{‡, b} Daire J. Cott,^c Sara Bals^b and Christophe Detavernier^{a, *}

Porous metal oxides with nano-sized features attracted intensive interest in recent decades due to their high surface area which is essential for many applications, e.g. Li ion batteries, photocatalysts, fuel cells and dye-sensitized solar cells. Various approaches were so far investigated to synthesize porous nanostructured metal oxides, including self-assembly and template-assisted synthesis. For the latter approach, forests of carbon nanotubes are considered as particularly promising templates, with respect to their one dimensional nature and the resulting high surface area. In this work, we systematically investigate the formation of porous metal oxides (Al_2O_3 , TiO_2 , V_2O_5 and ZnO) with different morphologies using atomic layer deposition on multi-walled carbon nanotubes followed by post deposition calcination. X-ray diffraction, scanning electron microscopy accompanied with X-ray energy dispersive spectroscopy and transmission electron microscopy were used for the investigation of morphological and structural transitions at the micro- and nano-scale during the calcination process. The crystallization temperature and the surface coverage of the metal oxides and the oxidation temperature of the carbon nanotubes were found to produce significant influence on the final morphology.

Introduction

Porous metal oxide nanostructures with high surface area are attractive for photocatalysis, dye-sensitized solar cells and lithium ion batteries applications and have been investigated intensively in recent years.¹⁻³ Atomic layer deposition (ALD) is a powerful tool to deposit ultrathin metal oxide films of high quality and offers the possibility of decorating porous materials with very thin coatings due to its self-limited reaction mechanism.⁴ Various porous nanostructures can therefore be synthesized through ALD onto different porous templates such as peptide, anodized alumina, nanofibrillar aerogels, mesoporous block copolymer and multi-walled carbon nanotubes (MWCNTs). After template removal, TiO_2 nanotubes, RuO_2 nanotubes, Pt nanotubes, interconnected hollow metal oxide nanotubes and 3D network of Pt nanowires were successfully synthesized.⁵⁻¹⁰ Usually, the removal of the CNTs results in hollow metal oxide tubes, as expected based on the uniform and conformal nature of the ALD technique. However, in our previous work, we demonstrated the synthesis of photocatalytically active TiO_2 nanoparticle chains forests by coating MWCNTs with TiO_2 using ALD and subsequent calcination to remove the carbon.¹¹ The resulting material offered a high photocatalytic activity towards the degradation of acetaldehyde under UV light.¹² Such morphological transformation from a tubular coating deposited onto MWCNTs into the chains of TiO_2 nanoparticles is dramatically different from the expected morphology of hollow oxide nanotubes and therefore warrants further investigation. In this work, we systematically studied the calcination of ALD-coated vertical aligned MWCNTs and investigated the kinetics of the carbon removal and the morphological and structural changes at the micro- and nano-scale before and after calcination.

Experimental section

MWCNTs were synthesized by plasma enhanced chemical vapor deposition (PECVD). 70nm TiN and 1nm Co as catalyst for MWCNT growth were sputtered on 8-inch Si wafer (Endura PVD tool, Applied Materials, USA). A 5 minutes NH_3 plasma treatment for the Co transformed the film into active metal nanoparticles to grow MWCNTs. $\sim 6.5\mu\text{m}$ MWCNTs were grown in a microwave (2.45 GHz) PECVD (TEL, Japan) by using a $\text{C}_2\text{H}_4/\text{H}_2$ mixture gas at a temperature $>550^\circ\text{C}$ for 30mins. The MWCNTs were then loaded into a homemade ALD system with a base pressure of 2×10^{-7} mbar. Metalorganic precursors and ozone were alternatively pulsed into the chamber while the MWCNTs sample was heated up to 100°C for TiO_2 , ZnO and Al_2O_3 and 150°C for VO_x . Tetrakis-(dimehtylamido) titanium (TDMAT) (99.9%, Sigma Aldrich), Tetrakis-(ethylmethylamino) vanadium (TEMAV) (Air Liquide), Diethylzinc (DEZn) (≥ 52 Wt%, Sigma Aldrich) and Trimethylaluminum (TMA) (97%, Sigma Aldrich) were used as metal precursors for TiO_2 , VO_x , ZnO and Al_2O_3 , correspondingly. To achieve a conformal coating on the MWCNTs forest, 20-30 seconds precursor pulses at a pressure of 0.4~0.5 mbar were applied. The pumping time was chosen as twice the pulse time to ensure sufficient evacuation of the residual precursor vapor and reaction products, thus avoiding chemical vapor deposition inside the films. After ALD coating, the samples were calcined with a ramp rate of 5°C per min to remove the carbonaceous template. *In situ* x-ray diffraction (adapted Bruker D8 system) was used to characterize the crystallization behavior during the calcination. Scanning electron microscopy (SEM) accompanied with energy dispersive X-ray spectroscopy (EDXS) was performed using a FEI Quanta 200 F to resolve the morphology of the samples before and after annealing. TEM specimens were prepared by scraping off the films from the silicon substrate surface and suspending the resulting product in ethanol. A drop of this suspension was deposited on a carbon coated TEM grid. Bright-field TEM (BFTEM) and high-resolution TEM (HRTEM) images as well as selected area electron diffraction (SAED) patterns were collected using a FEI Tecnai F20 operated at 200 kV. Energy filtered TEM (EFTEM) elemental maps

were obtained using a Philips CM30-FEG microscope operated at 300 kV. In addition, the crystallization temperature of metal oxide and oxidation temperature of MWCNTs were defined as T_{cry} and T_{ox} , respectively.

Results and discussion

Forests of MWCNTs with a thickness of $\sim 6.5\mu\text{m}$ were coated with 100 cycles of Al_2O_3 , TiO_2 , ZnO and VO_x , respectively. After ALD, these samples were respectively calcined at 600°C , 500°C , 450°C and 450°C in air for 3 hours to remove the carbon. In Fig. 1, SEM images show that all samples still exhibit a forest-like structure at the micro-scale upon calcination. The thicknesses of Al_2O_3 , TiO_2 and VO_x coated CNTs forests films are similar to the original thickness of the as-grown MWCNTs ($\sim 6.5\mu\text{m}$), but there is a noticeable shrinkage of the ZnO film ($\sim 4.7\mu\text{m}$). With the exception of the minor changes in their thicknesses, there is no remarkable collapse observed in these films. The EDS results of the calcined samples shown in Fig. 1 (f)-(i) indicate that these metal oxide forests are free standing nanostructures without the carbon support. In the following, we will analyze their nano-scale morphology before and after calcination, and try to unveil the kinetics case by case using TEM and EDXS.

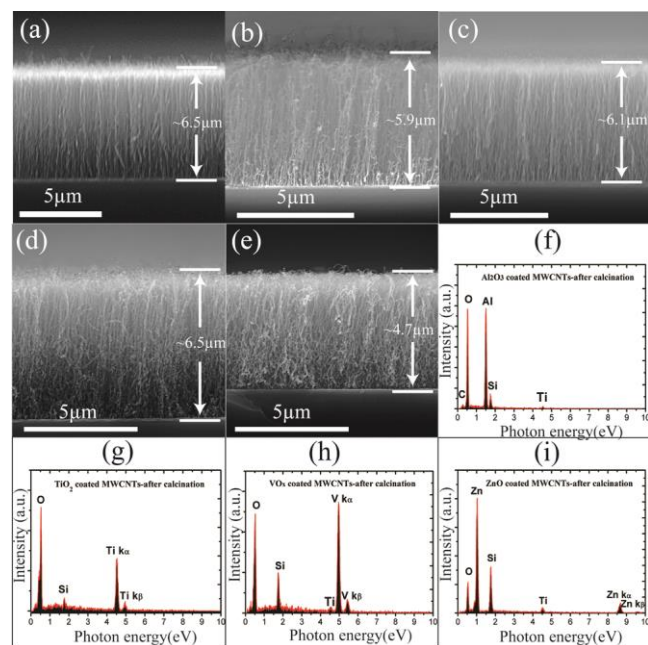


Fig.1 (a) shows the SEM image of TiO_2 coated MWCNTs before calcination. (b), (c), (d) and (e) SEM images show the Al_2O_3 , TiO_2 , VO_x and ZnO coated MWCNTs after annealing in air. (f), (g), (h) and (i) show the EDXS results from (b), (c), (d) and (e), respectively.

a. Al_2O_3 hollow nanotubes

Detailed TEM study combined with EFTEM elemental mapping applied to the as deposited Al_2O_3 coated MWCNTs sample shows that a uniform layer of amorphous Al_2O_3 was deposited on the surface of the MWCNTs (see Fig.2 (a)-(d)). The HRTEM image in Fig. 2(a) shows that the thickness of the Al_2O_3 coating on MWCNTs is smaller than a few nanometers. The uncoated section of the

MWCNT indicated in Fig. (e) by a circle in the color-coded EFTEM elemental map might be due to overlapping of neighboring MWCNTs during the deposition which encumbered the exposure of this section to the precursors. After the deposition, the sample was annealed at 600°C in air for 3 hours to remove the MWCNTs. As can be seen in Fig. 2 (e), hollow Al_2O_3 nanotubes were formed successfully. The calcination process appears to have no effect on the tubular morphology, which is in agreement with an earlier work.¹¹

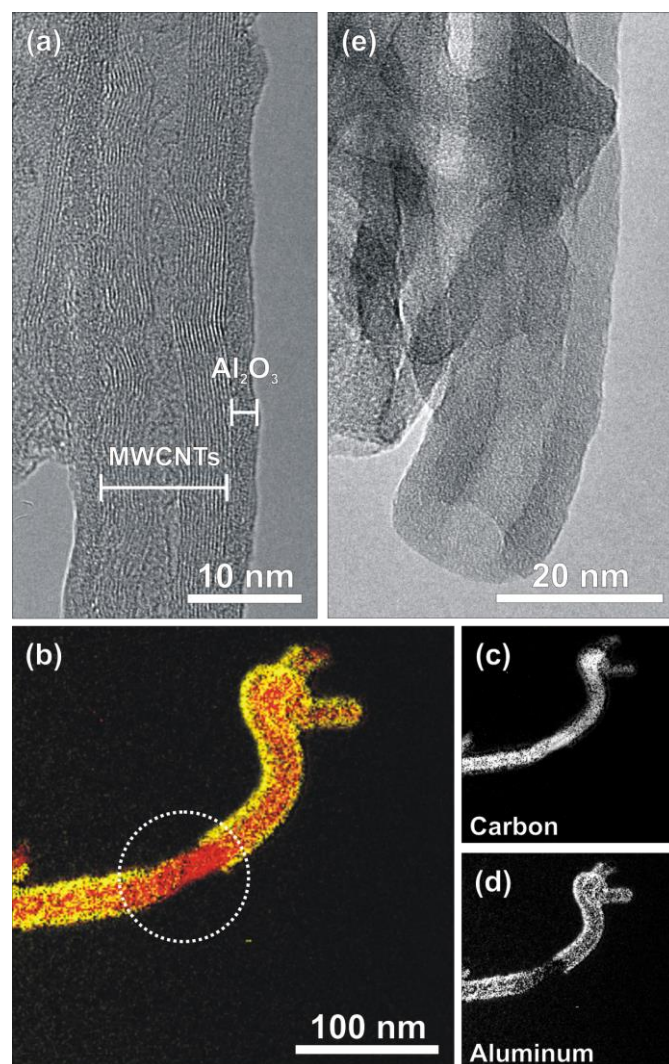


Fig.2 The amorphous Al_2O_3 coating and the graphitic layers of the MWCNTs are visible on the HRTEM image in (a). The carbon and aluminum contents of the nanotubes are presented in (b) showing the color-coded EFTEM map generated from individual (c) carbon (red) and (d) aluminum (yellow) elemental maps. A white circle in Fig. 2 (b) indicates a part that is not coated by Al_2O_3 . TEM image of Al_2O_3 nanotubes after annealing in air at 600°C for 3 hours is given at (e).

b. TiO_2 nanoparticle chains

Calcination of MWCNTs coated with continuous TiO_2 layers resulted in a remarkably different morphology at the nano-scale compared to MWCNTs coated with Al_2O_3 after the carbon removal. Fig. 3 (a) indicates that prior to calcination, a continuous layer of amorphous TiO_2 is present at the MWCNTs. After the calcination, the TiO_2 coating surrounding the MWCNTs transform into TiO_2

nanoparticles that are interconnected to each other. Fig.3 (b) indicates that these TiO_2 nanoparticles are fully solid and crystallized (e.g. not hollow). To understand the evolution of this transformation, detailed HRTEM characterization accompanied with chemical elemental mapping was carried out on samples that were quenched at different temperatures during calcination. According to the results of *in situ* XRD, the temperature of crystallization (T_{cry}) of ALD TiO_2 coating is $\sim 400^\circ\text{C}$.¹¹ Thus, a series of samples were by taking quenches at 400, 425, 450 and 475°C for HRTEM characterization. In this manner, the morphologic transformation during calcination can be investigated. HRTEM images show that until 475°C , the MWCNTs are still intact. However, for the sample quenched at 475°C (Fig. 3 (c)-(g)), the carbon content starts to decrease remarkably. As can be seen in Fig.3 (f) and (e), only a small amount of carbon is present inside the nanotube (indicated by white arrows). It should be here noted that the intense carbon signal observed at the carbon elemental map (indicated by red arrows) stems from the holey carbon of the TEM grid. On the other hand, the TiO_2 coating retains its tubular shape. This indicates that the carbon removal precedes the morphologic transformation. Fig. 3 (c) shows that even though the TiO_2 coating is still surrounding the partly removed MWCNTs, the coating starts to transform from amorphous to continuous and waved crystallized sections, with a rougher surface than the as deposited sample. As shown in Fig. 3 (d), some hollow TiO_2 nanotubes already appear.

XRD results on these samples further reveal that the TiO_2 coating started to crystallize at a temperature between 400 and 425°C and this crystallization proceeded more intensely at higher temperatures (Fig.4). It was expected that the calcination at 500°C for 3 hours is necessary to fully crystallize the TiO_2 . From the HRTEM analysis, we know that the transformation of TiO_2 from tubular coating to nanoparticles started from $\sim 475^\circ\text{C}$, which is higher than the oxidation temperature (T_{ox}) of MWCNTs, which will be discussed further later on. Upon exceeding this temperature, the crystallized TiO_2 sections began to sinter into interconnected nanoparticles when the MWCNTs were fully removed, causing the tubular morphology to collapse into chains of crystallized nanoparticles. Comparing with previous results of Al_2O_3 coated nanotubes, we can conclude that the lower T_{cry} of TiO_2 allows the sintering of crystallized TiO_2 into nanoparticles instead of maintaining a tubular morphology. The thickness of the coating and the diameter of the MWCNT are also important parameters in determining the final morphology. When the coating is too thick, the merging of TiO_2 crystalline grains into nanoparticles is not likely to take place since the tubular coating is thick enough to maintain its own structure. Also, when the tube is too thick, it will be more difficult for the metal oxide walls to merge together.^{7, 14, 15}

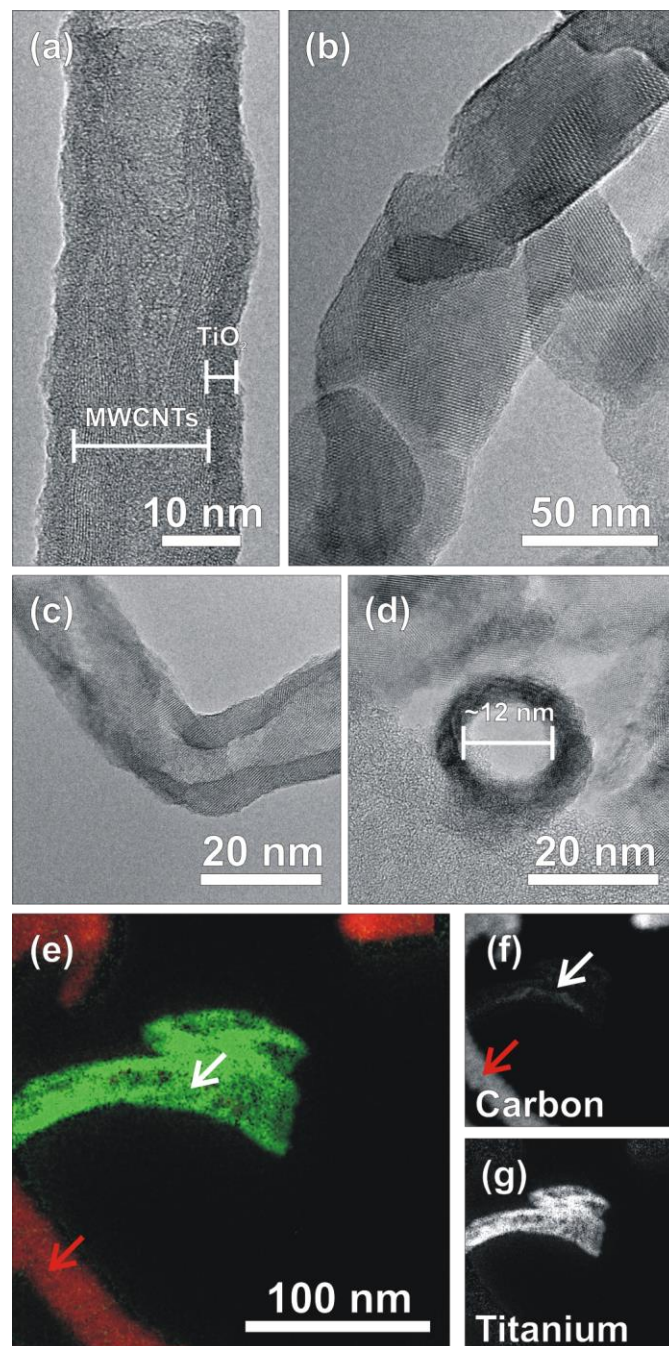


Fig.3 The amorphous TiO_2 coating and the graphitic layers of the MWCNTs are visible on the HRTEM image in (a). HRTEM images (b) of TiO_2 coated MWCNTs after calcination reveals the crystalline TiO_2 nanoparticle chains. (d) HRTEM images (c) and (d) of 475°C quenched sample show tubular morphology. The carbon (red) and titanium (green) contents of the nanotubes are presented in (e) showing the color-coded EFTEM map generated from individual (f) carbon and (g) titanium elemental maps.

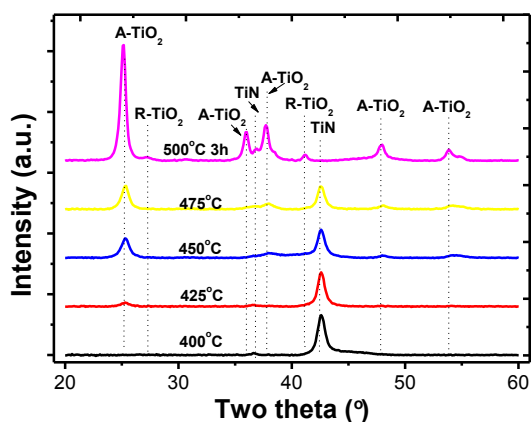


Fig. 4 XRD patterns of 400, 425, 450, 475°C quenched and 500°C calcined for 3 hours TiO₂ coated MWCNTs samples. A-TiO₂ and R-TiO₂ stand for TiO₂ of the anatase and rutile phase, respectively.

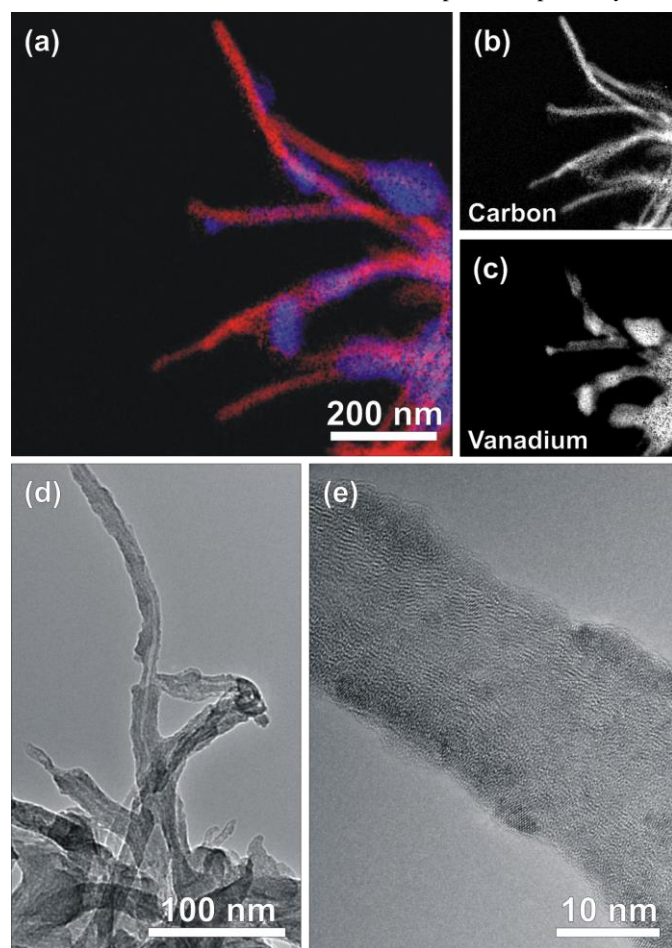


Fig. 5 The carbon and vanadium contents of the nanotubes are presented in (a) showing the color-coded EFTEM map generated from individual (b) carbon (red) and (c) vanadium (dark blue) elemental maps. TEM image at (d) depicts the uncoated and coated MWCNTs after ALD VO_x. (e) HRTEM image reveal crystalline VO_x coatings in some spots prior to calcination (c).

c. V₂O₅ and ZnO network of interconnected nanoparticles

When applying ALD on MWCNTs to synthesize porous metal oxides, the homogeneity of the initial coating is usually considered to be crucial for preserving the whole structure after carbon removal.¹⁶ If the metal oxide coating is discontinuous, the whole structure is generally expected to collapse after the carbon removal. However, the following results of synthesizing porous V₂O₅ and ZnO nanostructures using the same approach employed above show that a continuous and homogeneous coating is in fact not indispensable for structural preservation. HRTEM characterizations together with element mapping on 100 ALD cycles of VO_x or ZnO coated MWCNTs show that ALD resulted in a non-uniform coating of VO_x or ZnO on the surface of the MWCNTs, which is due to the inhomogeneity of the MWCNTs.^{17, 18} Fig. 5 (a)-(c) show VO_x layers on parts of the MWCNTs, whereas other sections remained uncoated (Fig. 5 (b)). The HRTEM image in Fig. 5 (e) shows that in some regions, the as deposited VO_x coating has already crystallized into the V₂O₅ phase. ALD of ZnO on MWCNTs shows similar results. ZnO nanoparticles are attached to the surface of MWCNTs (see Fig. 6 (a)-(d)). The coverage of ZnO on the MWCNTs is even less than for VO_x. Fig. 6 (d) shows that the ZnO nanoparticles are already crystallized as deposited.

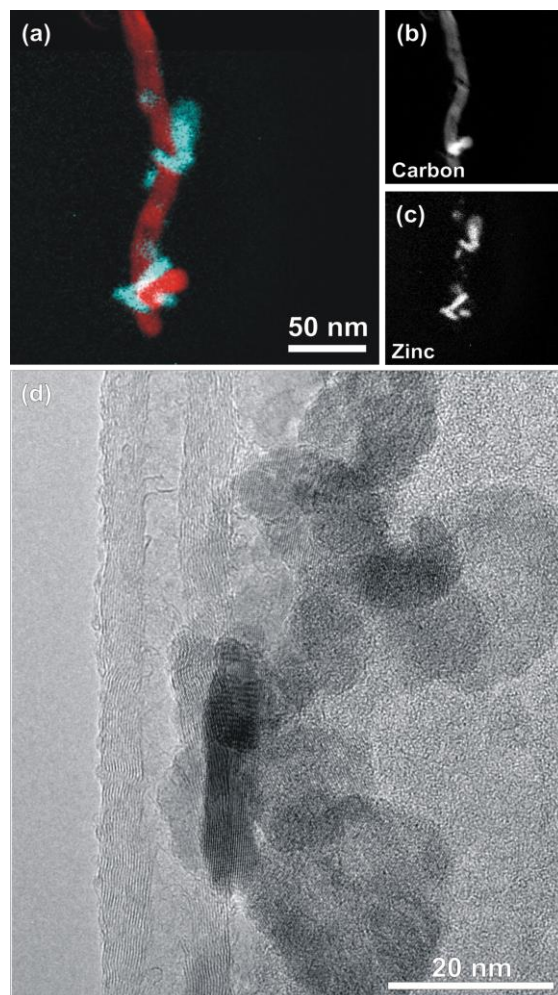


Fig. 6 The carbon and zinc contents of the nanotubes are presented in (a) showing the color-coded EFTEM map generated from individual (b) carbon (red) and (c) zinc (light blue) elemental maps. (d) HRTEM image reveals crystallized ZnO nanoparticles attached to the surface of MWCNTs.

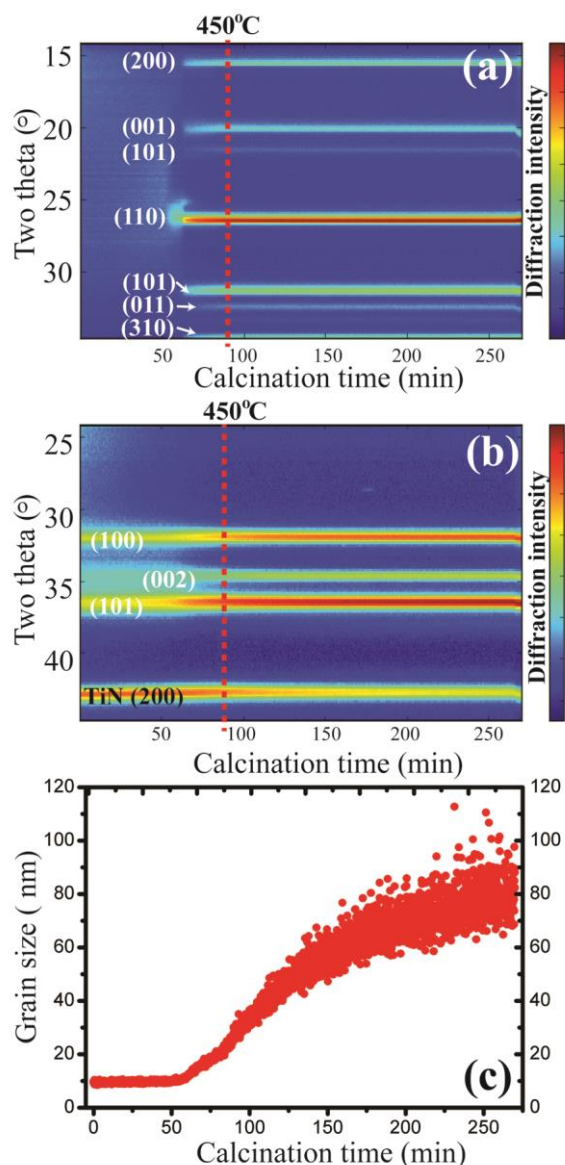


Fig.7 *In situ* XRD of VO_x (a) and ZnO (b) coated MWCNTs annealed from 20 to 450°C with a ramp rate of 5°C per min and stay at 450°C for 3 hours. The grain size of ZnO versus calcination time is shown in (c), calculated from *in situ* XRD data using the Scherrer equation.

In order to remove the carbon, these samples were calcined at 450°C in air for 3 hours. SEM images in Fig. 1 (e) and (f) show that after the calcination, the VO_x and ZnO samples still exhibit a similar forest like morphology at the micro-scale. The VO_x forest has the same overall thickness of ~6.5 μm as the original MWCNTs, whereas the ZnO slightly shrinks to ~4.7 μm. However, in spite of the particle-type nature of the metal oxide ALD coating, the structures do not collapse or disintegrate upon removal of carbon.

In situ XRD was used to monitor the crystallization behavior of these metal oxides when calcining these films from room temperature to 450°C. VO_x crystallized into V₂O₅ at approximately T_{cr}=290°C and showed no increase in grain size after crystallization (Fig. 7 (a)), whereas ZnO coatings did not show remarkable changes of the diffraction peaks during calcination since they were already crystallized as deposited (Fig.7 (b)). However, a notable intensification of the diffraction peaks of ZnO (100), (002) and (101)

was observed in Fig.7 (b), which implies that there was an increase in the grain size of the ZnO coating. Basing on the evolution of the diffraction peak at (101), we used the Scherrer equation to plot the variation of grain size versus calcination time, as shown in Fig.7 (c). The result shows that the initial grain size of the as deposited ZnO was about 10nm and started to remain stable when the temperature reaches ~270°C. As the calcination temperature increases, the ZnO grains grow, which implies a merging process of ZnO nanoparticles during the calcination.

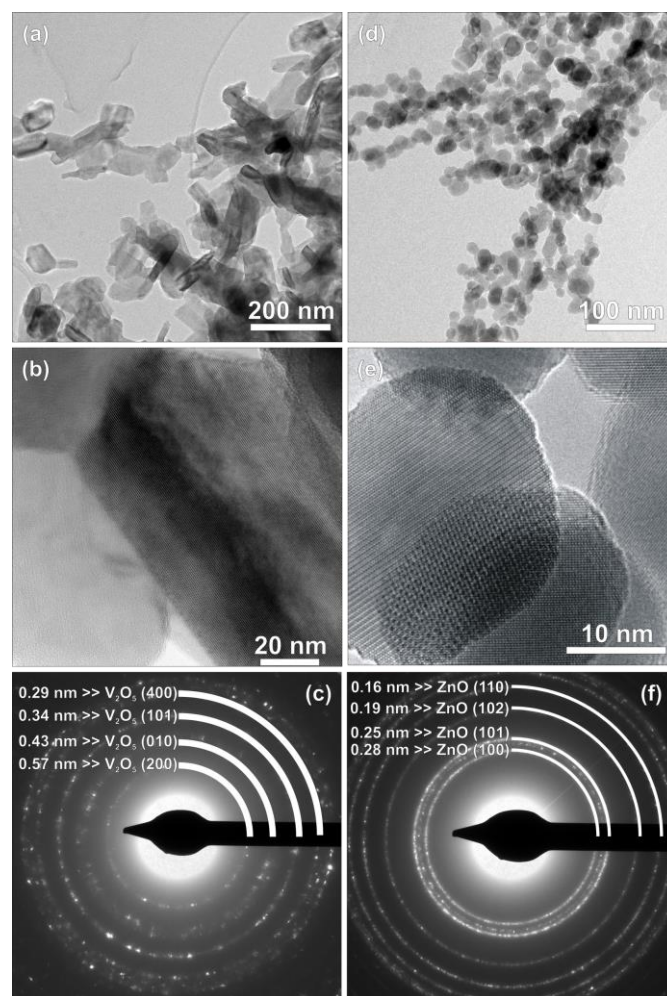


Fig.8 HRTEM images of the interconnected V₂O₅ nanorods after annealing VO_x coated MWCNTs in air (a-b). SAED pattern of crystallized V₂O₅ is shown in (c). HRTEM images of the interconnected ZnO nanoparticles after annealing ZnO coated MWCNTs in air (d) and (e). SAED pattern of crystallized ZnO is shown in (f).

To investigate the morphology of the VO_x and ZnO coatings after the calcination, HRTEM was carried out for these two films. Fig. 8 (a)-(b) show that the VO_x coating crystallizes into interconnected V₂O₅ nanorods, with diameter of 20 to 80nm and lengths of 60nm to more than 100nm. The electron diffraction rings in the selected area electron diffraction (SAED) pattern of crystallized VO_x shown in Fig. 8 (c) is indexed according to the various planes of the V₂O₅ phase. In the case of ZnO, as shown in Fig. 9 (a) and (b), spherical ZnO nanoparticles with diameters from 10-50nm connect to each other in a similar manner as the V₂O₅ nanorods, indicating that during the carbon removal the initial separate nanoparticles connected to each

other and grew into larger particles. The SAED pattern in Fig. 9 (c) confirms that these ZnO nanoparticles are crystalline. The coverage of ZnO nanoparticles on MWCNTs is lower in comparison to the coverage for VO_x , explaining the shrinkage in the thickness (from ~ 6 to $\sim 4.7\mu\text{m}$) of the film after calcination compared to the film of V_2O_5 nanorods, as shown in Fig.1. Even though a uniform coverage of metal oxide on the MWCNTs may facilitate structure preservation during carbon removal, the examples of VO_x and ZnO clearly demonstrate that calcination of samples with a non-continuous coating can also result in a supportless nanostructure of porous metal oxide through merging and sintering of the separate nanoparticles into 3D interconnected networks during the calcination.

d. Kinetics of carbon removal

We systematically investigated the oxidation temperatures of MWCNTs coated with Al_2O_3 , TiO_2 , ZnO and VO_x by using EDXS to record the carbon signal at different quenches of the samples during calcination, as shown in Fig. 9 and 10. In Fig. 9, MWCNTs were coated with 100 ALD cycles of Al_2O_3 , TiO_2 , ZnO and VO_x respectively and annealed from room temperature to 600°C . Several quenches at different temperatures with 50°C intervals were preferred for EDXS measurement. For pure MWCNTs without metal oxide coating, T_{ox} is found to be $\sim 500^\circ\text{C}$. Upon coating with metal oxides, T_{ox} of MWCNTs changes accordingly. TiO_2 and VO_x coated MWCNTs have a $\sim 50^\circ\text{C}$ decrease in T_{ox} whereas for ZnO coated MWCNTs T_{ox} shows a $\sim 100^\circ\text{C}$ decrease.^{16, 19} However, a $\sim 50^\circ\text{C}$ increase of T_{ox} is observed for the Al_2O_3 coated samples.

Different numbers of ALD cycles were also applied to investigate the effect of the thickness of the metal oxide coating on T_{ox} . In Fig. 10, the carbon signal measured by EDS for 50, 100 and 200 cycles TiO_2 and Al_2O_3 coated MWCNTs are shown. For TiO_2 coated MWCNTs, the T_{ox} are independent of the thickness of TiO_2 . For the Al_2O_3 coated MWCNTs, the thicker the Al_2O_3 layer, the higher the T_{ox} . For 200 cycles of Al_2O_3 , removal of the carbon is not yet complete, even though the quench is taken at 650°C . The decrease in T_{ox} of MWCNTs can be attributed to the catalytic effect of coated metal oxides. Aksel et al proposed a possible mechanism of explaining this catalytic effect.¹⁶ First the oxygen in the metal oxide reacts with the carbon of the MWCNTs and generates CO and an oxygen vacancy in the metal oxide layer. Then oxygen vacancies will migrate to the gas-solid interface and be occupied with oxygen from the ambient. The results shown in Fig.9 are in agreement with this hypothesis. However, the results in Fig.10 show that the uniformity of the thin film coating also influences the oxidation temperature. If the layer of metal oxide is not dense enough e.g. TiO_2 compared to Al_2O_3 , increasing the thickness does not increase the oxidation temperature of the MWCNTs, since pin holes probably allow oxygen vacancies to migrate to the gas-solid interfaces. Comparing Fig.2 (a) with Fig. 3(a), the TiO_2 coating on the MWCNTs is less uniform than the Al_2O_3 , which implies that the uniformity and the quality of Al_2O_3 coating is better than TiO_2 and would have fewer pin holes. On the other hand, compared to other methods of coating metal oxides on MWCNTs, ALD is a well-known technique for growth of higher quality of metal oxides. Given perfect starting surface, ALD will grow metal oxide layer with limited pinholes. An increase of oxidation temperature was found when TiO_2 was deposited by ALD on oxygen plasma treated MWCNTs, which have more defective surface and are easier for TiO_2 to nucleate and form ALD coating with higher quality.¹⁸

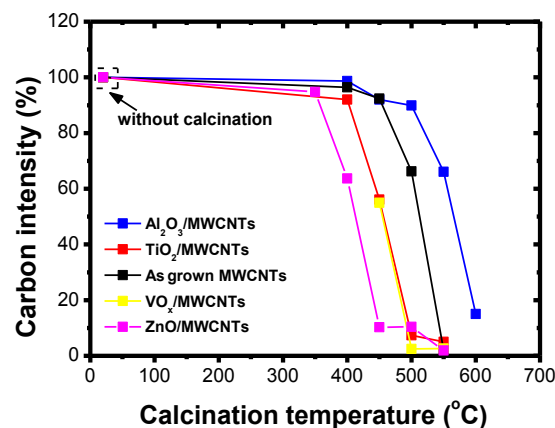


Fig. 9 EDXS measured carbon contents of Al_2O_3 , TiO_2 , VO_x and ZnO coated MWCNTs with 100 ALD cycles quenched at different temperatures. The result of referenced uncoated MWCNTs is also shown.

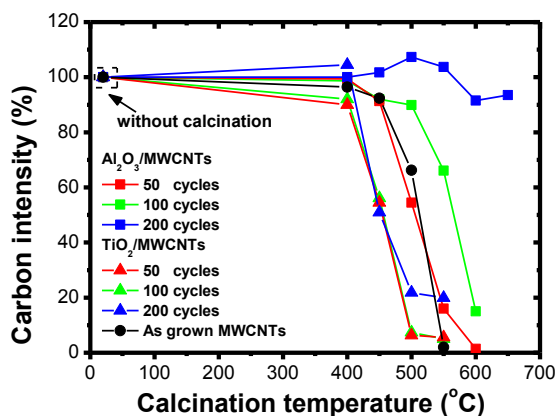


Fig.10 EDXS measured carbon contents of Al_2O_3 and TiO_2 coated MWCNTs with 50, 100 and 200 ALD cycles quenched at different temperatures. The result of referenced uncoated MWCNTs is also shown.

Conclusion

To summarize, by combining ALD metal oxides on MWCNTs and subsequent calcination, porous nanostructured metal oxides were successfully synthesized. A schematic illustration combined with TEM images is given in Fig. 11. The process of morphologic transformation during calcination is sketched according to T_{cry} and T_{ox} , as indicated in the scheme. From the systematic investigation above we can conclude that:

- For crystalline oxides (i.e. when calcining at temperatures higher than T_{cry}), sintering becomes a key mechanism during the calcination and determines the final morphology. For the TiO_2 sample, the driving force to reduce the surface area in combination with a sufficient mobility of the atoms causes a collapse of the hollow tube nanostructure into chains of anatase nanoparticles.
- As illustrated by the examples of VO_x and ZnO, a continuous coating of the MWCNTs is not indispensable for avoiding the entire structure to collapse during the removal of the carbon support. Self-supported, interconnected 3D structure can be

formed by merging and sintering of the initial separate nanoparticles during the calcination.

- iii. The uniformity and thickness of the metal oxide coating affects the T_{ox} of the MWCNTs. Thick layers of metal oxide with high quality increase the T_{ox} , which is due to the retardance of

oxygen vacancy diffusion from carbon-metal oxide interface to the exterior surface.

Summary of morphological transformation during calcination

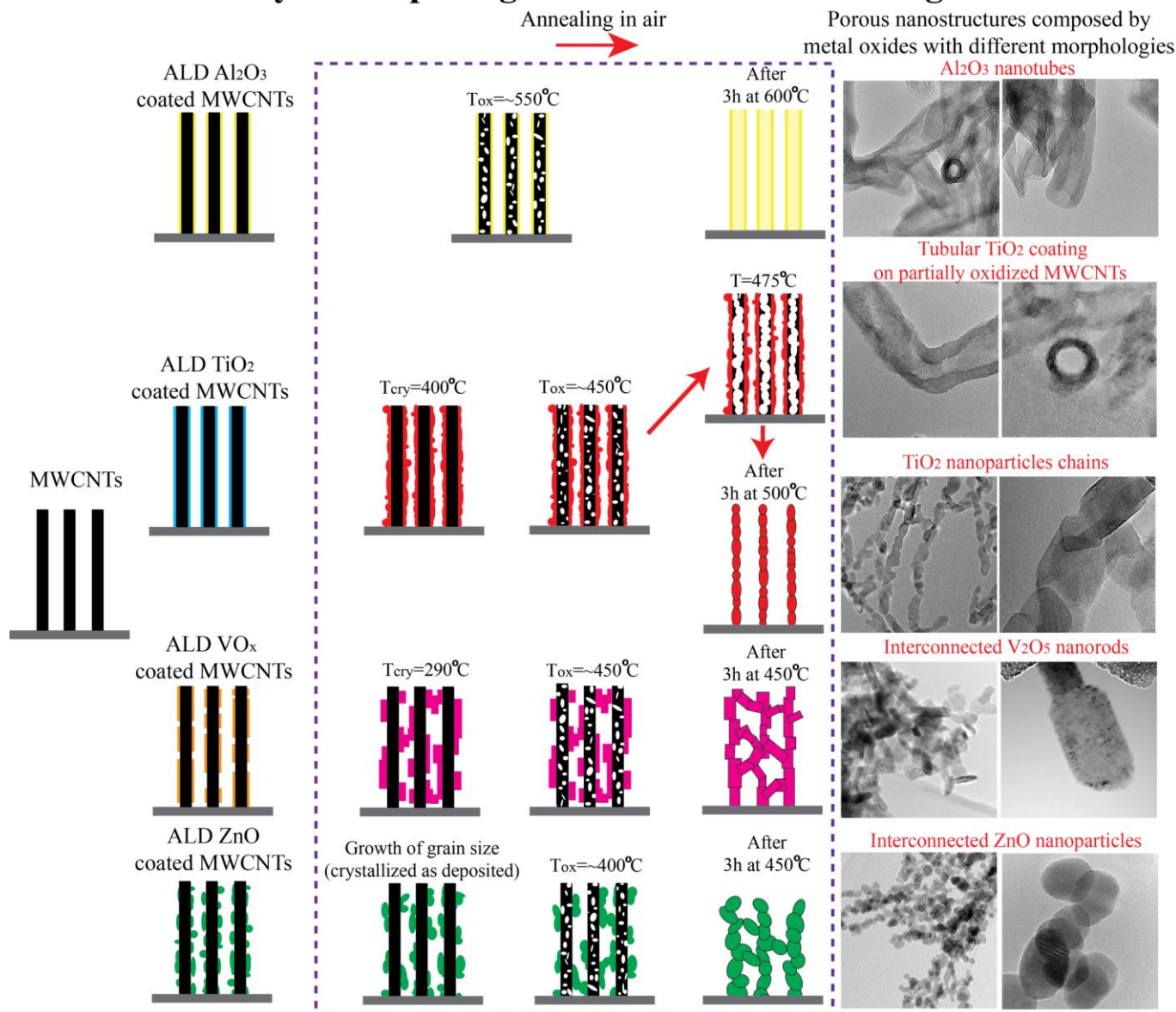


Fig. 11 Schematic demonstration of the formation of porous metal oxide nanostructures by ALD on MWCNTs followed by calcination.

Acknowledgements

The authors wish to thank the Research Foundation - Flanders (FWO) for financial support. The authors acknowledge the European Research Council for funding under the European Union's Seventh Framework Programme (FP7/2007-2013)/ERC grant agreement N°239865-COCOON and N°335078-COLOURATOMS. The authors would also want to thank the support from UGENT-GOA-01G01513 and IWT-SBO FUNC (STM-Vlaanderen).

Notes and references

^aDepartment of Solid State Sciences, Ghent University, Krijgslaan 281/S1, B-9000 Ghent, Belgium

^bDepartment of Physics, Electron Microscopy for Materials Science (EMAT), University of Antwerp, Groenenborgerlaan 171, B-2020 Antwerp, Belgium

^cIMEC, Kapeldreef 75, B-3001 Leuven, Belgium

‡These authors contributed equally.

- 1 Y. Li, Z.-Y. Fu, B.-L. Su, *Adv. Fun. Mater.* 2012, **22**, 4634-4667.
- 2 S. Agarwala, M. Kevin, A. S. W. Wong, C. K. N. Peh, V. Thavasi, G. W. Ho, *ACS Appl. Mater. Interfaces* 2010, **2**, 1844-1850
- 3 F. Cheng, Z. Tao, J. Liang, J. Chen, *Chem. Mater.* 2008, **20**, 667-681
- 4 C. Detavernier, J. Dendooven, S. P. Sree, K. F. Ludwig, J. A. Martens, *Chem. Soc. Rev.* 2011, **40**, 5242-5253.
- 5 S.-W. Kim, T. H. Han, J. Kim, H. Gwon, H.-S. Moon, S.-W. Kang, S. O. Kim, K. Kang, *ACS Nano*, 2009, **3**, 1085-1090.
- 6 Y.-S. Min, E. J. Bae, K. S. Jeong, Y. J. Cho, J.-H. Lee, W. B. Choi, G.-S. Park, *Adv. Mater.* 2003, **15**, 1019-1022.
- 7 D. J. Comstock, S. T. Christensen, J. W. Elam, M. J. Pellin, M. C. Hersam, *Adv. Fun. Mater.* 2010, **20**, 3099-3105
- 8 J. T. Korhonen, P. Hiekkataipale, J. Malm, M. Karppinen, O. Ikkala, R. H. A. Ras, *ACS Nano*, 2011, **5**, 1967-1974
- 9 F. Li, X. Yao, Z. Wang, W. Xing, W. Jin, J. Huang, Y. Wang, *Nano Lett.* 2012, **12**, 5033-5038
- 10 S. Deng, M. Kurttepel, S. Deheryan, D. J. Cott, P. M. Vereecken, J. A. Martens, S. Bals, G. Van Tendeloo, C. Detavernier, *Nanoscale*, 2014, **6**, 6939.
- 11 S. Deng, S. W. Verbruggen, Z. He, D. J. Cott, P. M. Vereecken, J. A. Martens, S. Bals, S. Lenaerts, C. Detavernier, *RSC Advances*, 2014, **4**, 11648
- 12 S. W. Verbruggen, S. Deng, M. Kurttepel, D. J. Cott, P. M. Vereecken, S. Bals, J. A. Martens, C. Detavernier, S. Lenaerts, *Appl. Catal. B: Environ.* 2014, **160-161**, 204-210
- 13 J. S. Lee, B. Min, K. Cho, S. Kim, J. Park, Y. T. Lee, N. S. Kim, M. S. Lee, S. O. Park, J. T. Moon, *J. Crystal Growth*, 2003, **254**, 443-448.
- 14 Y. Yang, L. Qu, L. Dai, T. S. Kang, M. Durstock, *Adv. Mater.* 2007, **19**, 1239-1243.
- 15 N. Du, H. Zhang, B. Chen, X. Ma, Z. Liu, J. Wu, D. Yang, *Adv. Mater.* 2007, **19**, 1641-1645.
- 16 S. Aksel, D. Eder, *J. Mater. Chem.* 2010, **20**, 9149-9154.
- 17 J. M. Green, L. Dong, T. Gutu, J. Jiao, J. F. Conley, Y. Ono, *J. Appl. Phys.* 2006, **99**, 094308
- 18 C. Marichy, N. Pinna, *Coordination Chem. Rev.* 2013, **257**, 3232-3253.
- 19 M.-G. Willinger, G. Neri, A. Bonavita, G. Micali, E. Rauwel, T. Hertrich, N. Pinna, *Phys. Chem. Chem. Phys.* 2009, **11**, 3615-3622
- 20 J. Ronge, S. Deng, S. P. Sree, T. Bosserez, S. W. Verbruggen, N. Kumar Singh, J. Dendooven, M. B. J. Roeflaers, F. Taulelle, M. De Volder, C. Detavernier, J. A. Martens, *RSC Advances*, 2014, **4**, 29286